JOURNAL OF SOLID STATE CHEMISTRY 48, 376–387 (1983)

Defect Structures in the Brannerite-Type Vanadates: V. Phase Diagram of the Pseudo-Ternary MnV_2O_6–$LiVMoO_6$–MoO_3 System Comprising the $Mn_{1-x-y}Li_yO_xV_{2-2x-y}Mo_{2x+y}O_6$ Solid Solution

JACEK ZIÓŁKOWSKI,* KRYSTYNA KRUPA, AND KRZYSZTOF MOCAŁA

Institute of Catalysis and Surface Chemistry, Polish Academy of Sciences, 30-239 Kraków, ul. Niezapominajek, Poland

Received August 4, 1982; in revised form January 17, 1983

The phase diagram of the pseudo-ternary MnV_2O_6–$LiVMoO_6$–MoO_3 system has been determined with DTA and X-ray phase analysis. Its outstanding feature is the very large range of stability of the quaternary solid solution α-MLØ described by the formula $Mn_{1-x-y}Li_yØ_xV_{2-2x-y}Mo_{2x+y}O_6$ (Ø = cation vacancy), and crystallizing in the monoclinic brannerite-type structure. In this solution y may vary between 0 and 1, which corresponds to the entire miscibility of MnV_2O_6 and $LiVMoO_6$; x may change between 0 and x_{max} depending on y (if, e.g., y equals 0.00, 0.40, 0.84, or 1.00, x_{max} is 0.45, 0.28, 0.16, or 0.00, respectively). Depending on composition, α-MLØ is stable up to 540–710°C. Other features of the diagram, including the liquidus, are described in detail. The dependence of unit cell dimensions on composition of α-MLØ has been determined. On passing from MnV_2O_6 to $LiVMoO_6$, the lattice parameter b and unit cell volume increase, c and $c \sin \beta$ decrease, and a changes insignificantly. These changes are interpreted by taking into account the ionic radii of the components and the specific details of the brannerite-type structure. MLØ solid solutions were prepared using the amorphous citrate precursor method.

Introduction

For about thirty years oxide solid solutions have been the object of wide and ever-increasing interest from the viewpoint of both fundamental and applied science (materials chemistry, catalysis, etc.). This is due to the possibility of an infinite modification of their physical and chemical properties. The laws governing their formation have not, however, been fully established. This is so especially for the multicomponent oxide solutions of the oxysalt-type matrix.

In the present series of investigations, we have focused our attention on the solid solutions of MoO_3 in the matrices of metal vanadates AV_2O_6 crystallizing in the brannerite-type structure (*1–4*). So far we have indicated the existence of solid solutions described by the formulas

$$Mn_{1-x}Ø_xV_{2-2x}Mo_{2x}O_6 \ (0 \le x \le 0.45) (1)$$

and

$$Cu^{2+}_{1-x-y}Cu^{1+}_yØ_xV_{2-2x-y}Mo_{2x+y}O_6 \quad (0 \le x \le 0.23;\ 0 \le y \le 0.27) (3).$$

In these solutions Mo^{6+} ions are substituted at random for V^{5+} ions, and charge compensation is accomplished by creation of an

* To whom all correspondence should be addressed.

0022-4596/83 $3.00

equivalent number of cationic vacancies Ø at bivalent metal sites or by partial reduction. On the other hand, Galy and Darriet (*5*, *6*) have shown that the *A* position in the brannerite-type matrix may be entirely filled up with typically monovalent cation (e.g., $LiVMoO_6$); an increase of the Mo^{6+}/V^{5+} ratio results also in a deficiency of monovalent cation *A* (e.g., $Li_{1-x}Ø_xV_{1-x}Mo_{1+x}O_6$). The above-mentioned facts enabled us to set up a hypothesis concerning the possible existence of quaternary solid solution described by the formula $Mn_{1-x-y}Li_yØ_xV_{2-2x-y}Mo_{2x+y}O_6$ (further labeled as MLØ). This hypothesis is confirmed in the present paper.

The above-quoted $Mn_{1-x}Ø_xV_{2-2x}Mo_{2x}O_6$ (MØ) and $Li_{1-x}Ø_xV_{1-x}Mo_{1+x}O_6$ (LØ) solid solutions are special examples of the general MLØ formula at $y = 0$ and at $x + y = 1$, respectively, and belong correspondingly to the MnV_2O_6–MoO_3 and $LiVMoO_6$–MoO_3 subsystems. Similarly, at $x = 0$ one arrives at $Mn_{1-y}Li_yV_{2-y}Mo_yO_6$ (ML), which may be regarded as a solid solution made of $(1 - y)MnV_2O_6$ and $yLiVMoO_6$. The composition of MLØ thus falls within the pseudo-ternary MnV_2O_6–$LiVMoO_6$–MoO_3 section of the quaternary, tetrahedral composition diagram MnO–V_2O_5–MoO_3–Li_2O, shown in Fig. 1. The phase diagram of the above-mentioned pseudo-ternary system is resolved in the present paper, and (among others) the range of stability of α-MLØ solid solution is determined.

It has been found convenient to represent the composition of the above-mentioned pseudo-ternary system by means of the equilateral triangle configuration, formally using the MLØ formula over its whole area. Consequently, the composition parameters x (or $X = 100x$) and y (or $Y = 100y$) are used to express the composition along MnV_2O_6–MoO_3 and MnV_2O_6 and $LiVMoO_6$ arms of the triangle, respectively. The properties of such a diagram are shown in Fig. 1(b). In particular, the series of samples of constant concentration of Mn, Li, Ø, V, and Mo can be easily indicated as lying on the respective straight lines.

Experimental

The composition of all samples prepared and studied with DTA and X-ray analysis is marked in Fig. 3. They were synthesized by the amorphous citrate precursor method (*7*), adapted empirically to the present system. The method seems to be especially convenient for multicomponent systems, as

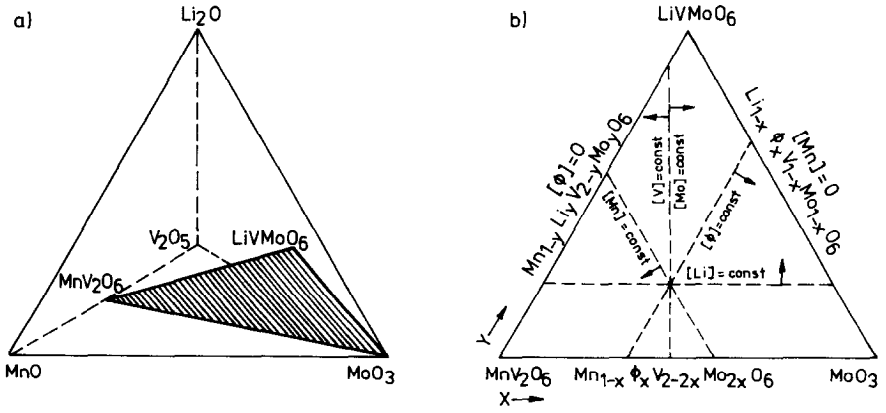

FIG. 1. (a) Location of the MnV_2O_6–$LiVMoO_6$–MoO_3 triangle in the MnO–Li_2O–V_2O_5–MoO_3 composition tetrahedron. (b) Properties of the equilateral composition triangle MnV_2O_6–$LiVMoO_6$–MoO_3. Arrows mark the direction in which the concentration of the respective component increases.

it assures very good homogenization. The starting materials were Li_2CO_3, $MnCO_3$, NH_4VO_3, $(NH_4)_6Mo_7O_{24} \cdot 4H_2O$, 0.1 M HNO_3, 2.5 M citric acid (CA), and 0.1 M ammonia, all of p.a. grade. Li, Mn, V, and Mo-containing salts were always weighted in the appropriate amounts, and CA was titrated in the quantity corresponding to the formation of lithium, manganese, or ammonium citrates.

Li_2CO_3 and $MnCO_3$ were first dissolved in HNO_3 taken in a little excess to the stoichiometry, CA was added and the solution was neutralized with ammonia (pH $\approx$ 7). The respective portions of ammonium vanadate and molybdate were added separately and dissolved on stirring at 70°C. Then water was entirely evaporated from the solution at 90°C, at pressures achieved with a water pump. The glasslike, amorphous, solid product was ground and heated in a stream of air at temperature increasing by 50° every 30 min, up to 550°C. The final thermal treatment consisted of annealing the samples in air at 550–600°C for 20 hr. Samples exhibiting the presence of MoO_3 in addition to the brannerite-type phase via X-ray analysis were additionally heated at the same temperature up to 100 hr (and again periodically tested with X-ray analysis), to be sure that real equilibrium had been reached. After annealing, samples were quenched to room temperature to freeze in the high temperature equilibrium state.

As for the selected preparations belonging to the MnV_2O_6–MoO_3 arm of the diagram, no differences were found between the properties of samples of the same composition prepared with presently applied citrate precursor method, as compared to solid state synthesis, employed in (*1*). All data concerning the samples of this arm are thus quoted from Ref. (*1*).

Among samples studied in this work the most interesting are those which fall in the stability range of the MLØ solid solution (cf. Fig. 3). Their color changes with composition. MnV_2O_6 is brownish-black; with increasing x in the MØ series up to $x = 0.45$ samples become brown or brownish-red. The same color changes occur with increasing y in the MLØ series up to about $y = 0.7$; however, these samples are somewhat paler compared to the former ones. At higher y color changes through green to yellow, characteristic of pure $LiVMoO_6$.

The X-ray diffraction patterns were obtained with DRON-2 X-ray diffractometer using CuKα radiation and an internal standard of Al (a = 4.0492 Å at 25°C). The phase identification was based upon the published patterns of MnV_2O_6 (*1*), $LiVMoO_6$ (*6*), and MoO_3 (*8*). The cell dimensions were refined by the least-squares method. Some details of the phase diagram described in the further paragraphs of this paper were confirmed by analysis in high-temperature X-ray camera. In this case the temperature was increased in the interesting range by 5 or 10° every 60 min.

DTA curves were recorded with a SE TARAM M5 microanalyzer in a stream of purified air, at a heating rate of 10°/min. Al_2O_3, preheated at 1500°C for 24 hr, and Brazilian quartz (transition temperature 573°C) were used as references. A specially constructed sample holder was used, as described in detail in (*1*). On constructing the phase diagram, the onset temperatures (determined with tangent method) and last peak temperatures were taken to determine the solidus and liquidus lines, respectively, the accuracy being ±2°C. The temperatures of usually overlapping, intermediary effects were estimated as exactly as possible, with an accuracy which should not be less than ±5°C. The DTA curves recorded on cooling (10°/min) indicated considerable overcooling; thus, they were not directly useful in constructing the phase diagrams. However, as the peaks were well separated, the cooling runs were frequently used to control the peak number. This was especially

useful in locating the peritectic lines (cf. Figs. 5–7, temperature range above 760°C). Tentative details of the phase diagrams are always indicated with dotted lines.

The magnetic susceptibility was measured between 120 and 290 K using the Gouy method as described in Refs. (*3, 9, 10*) using *tris*(ethylenediamine) nickel(II) thiosulfate as a calibration standard ($10^6\ \chi_g$ = 10.82 at 25°C) (*11*). The susceptibility, which was found to be independent of the field strength, was determined at H = 2 to 4 kOe. The correction for the susceptibility of the glass tube was determined experimentally, and the diamagnetic corrections were calculated according to Klemm's method (*12*). The reproducibility of the magnetic moment determination was estimated to be within $\pm 0.1\ \mu_B$.

Elemental analysis was carried out using atomic absorption spectroscopy (Pye Unicam FP 90 spectrometer) (Mn, V, Mo) or classical flame photometry (Li), the accuracy being ±1% in the absolute weight of the metals.

Results and Discussion

(*i*) *Verification of the MLØ Formula*

In analogy to the previously studied systems, the composition of MLØ solid solution in the MnV_2O_6–$LiVMoO_6$–MoO_3 system could be written as

$$Mn^{2+}_{1-x-y}Li^{1+}_{y}Ø_x V^{5+}_{2-2x-y}Mo^{6+}_{2x+y}O_6 \quad (1)$$

However, charge compensation could also occur by reduction of V^{5+} to V^{4+} or Mo^{6+} to Mo^{5+}. In the latter cases this would lead to the formulas

$$Mn^{2+}_{1-y}Li^{1+}_{y}V^{5+}_{2-2x-y}Mo^{6+}_{y}Mo^{5+}_{2x}O_6 \quad (2)$$

or

$$Mn^{2+}_{1-y}Li^{1+}_{y}V^{5+}_{2-4x-y}V^{4+}_{2x}Mo^{6+}_{2x+y}O_6. \quad (3)$$

To resolve this question elemental analysis and magnetic susceptibility measurements were executed for four selected samples: pure MnV_2O_6 (X = 0, Y = 0), (X = 30, Y = 0), (X = 30, Y = 30), and (X = 20, Y = 80). As will be shown below (cf. Fig. 3), in X-ray analysis all these samples exhibit the presence of only one brannerite-type phase, and thus all of them belong to the stability of MLØ.

An elemental analysis of the quoted samples, performed after final thermal treatment, has shown that all of them have the assumed stoichiometry, corresponding to the formula (1), within the error of analytical methods. This indicates that there was no loss of components in the course of heating. Let us remark that formulas (2) and (3) are richer in manganese (by xMn) as compared to (1). If solid solutions of (2)- or (3)-type had been formed in a mixture of composition (1), some of lithium, vanadium, and molybdenum should remain unconsumed in the form of simple oxides or salts. Simple stoichiometric calculations show that, e.g., sample (X = 20, Y = 60) would contain 51.3 weight% of phase (3), 1.8% of Li_2O, 18.1% of V_2O_5, and 28.7% of MoO_3. X-ray phase analysis clearly demonstrates that this is not the case, as the above-mentioned quantities markedly exceed the detectability limit of the method.

Figure 2 shows the results of magnetic measurements performed for four samples under discussion. $1/\chi$ vs T plots are linear, proving that the Curie–Weiss law is obeyed. The effective magnetic moment of Mn^{2+} ions, calculated on the assumption that formula (1) is valid, is practically the same for all four samples, and is equal to 5.65 ± 0.1 μ_B. The Weiss constant decreases along the series from 33 to 13 K, which may be due to the diminishing average distance between adjacent Mn^{2+} ions and the diminishing interactions between them. Let us remark that formulas (2) and (3) are richer in paramagnetic ions than (1) by (xMn^{2+} + 2xMo^{5+}) or (xMn^{2+} + 2xV^{4+}), respectively. If solid solutions of (2) or (3)

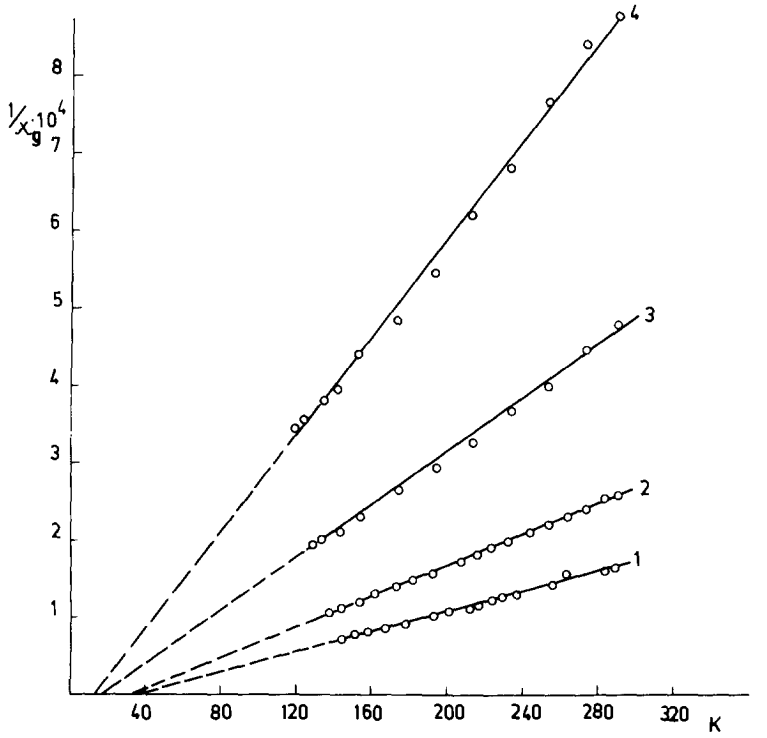

FIG. 2. Magnetic susceptibility of MnV_2O_6 and MLØ solid solutions as function of temperature. (1) MnV_2O_6, 5.65 μ_B θ = 33 K, (2) (X = 30, Y = 0), 5.55 μ_B, θ = 31 K, (3) (X = 30, Y = 30), 5.56 μ_B, θ = 17 K, (4) (X = 20, Y = 60), 5.75 μ_B, θ = 13 K.

type were formed in a mixture of composition (1), the apparent magnetic moment of Mn^{2+} calculated as for solution (1) should increase along the studied series of samples. Assuming, for instance, that solution (3) is formed, $\mu_{Mn^{2+}} = 5.65\ \mu_B$, $\mu_{V^{4+}} = 2\ \mu_B$ (*3*), and neglecting small changes in Weiss constant, one can estimate this apparent moment to be 5.65 μ_B for (X = 0, Y = 0), 5.86 μ_B for (X = 30, Y = 0), 5.95 μ_B for (X = 30, Y = 30), and 5.99 μ_B for (X = 20, Y = 60). The above effect is not observed experimentally. It is true that the expected differences in apparent $\mu_{Mn^{2+}}$ are rather small but they clearly exceed the possible experimental error (0.1 μ_B).

The experimental results discussed in this paragraph, and especially those of elemental analysis combined with X-ray phase analysis, prove that formula (1) is valid as a description of MLØ solid solutions.

(*ii*) *X-ray Studies*

Figure 3 presents the subsolidus portion of the pseudo-ternary MnV_2O_6–$LiVMoO_6$–MoO_3 phase diagram, as determined with X-ray phase analyses performed at room temperature (some details included in Fig. 3 and based on DTA will be explained in the next paragraph of the paper). As is seen, the range of stability of MLØ solid solutions of α (i.e., of brannerite-type) structure extends over about 50% of the triangular surface. Its other part corresponds to the coexistence of α-MLØ and MoO_3. The K_1K_2 line in Fig. 3 should be treated as indicating the composition of saturated solid

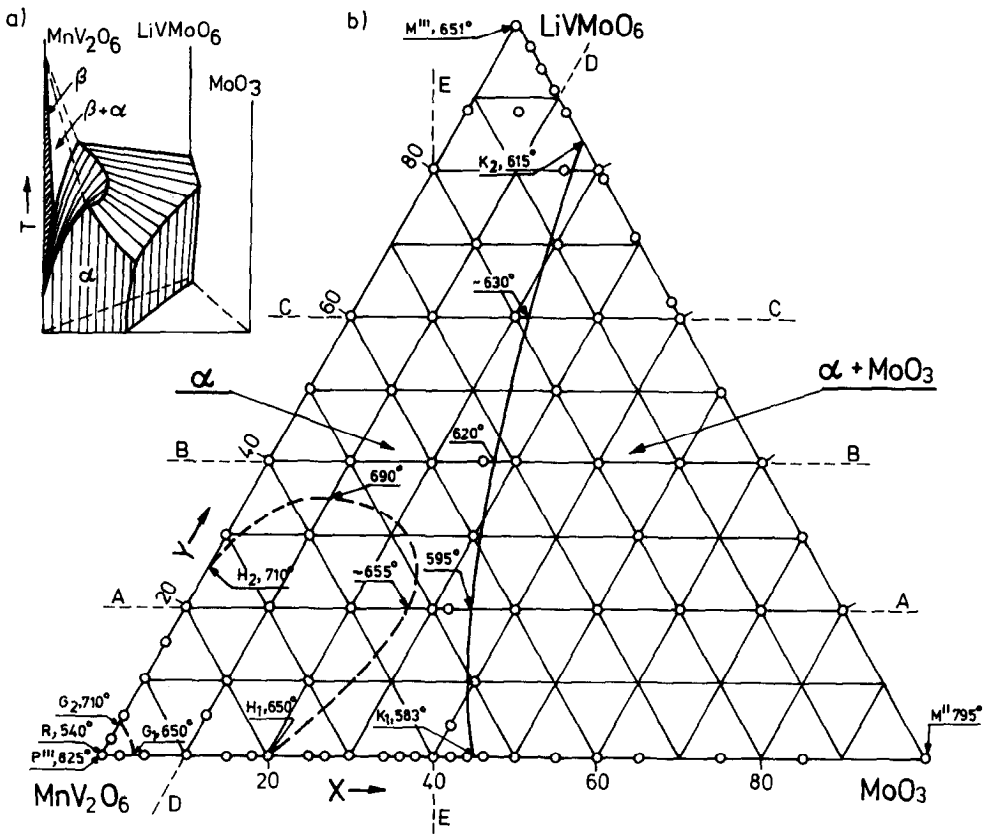

FIG. 3. Subsolidus portion of the phase diagram of the pseudo-ternary MnV_2O_6–$LiVMoO_6$–MoO_3 system. (a) Outline of the spaces of stability of α-MLØ and β-MLØ solid solutions. (b) Projection based on X-ray phase analysis and DTA (cf. Figs. 5–7). Temperature in °C. K_1K_2 borders on two areas of the subsolidus: α-MLØ and α-MLØ + MoO_3. H_1H_2 and G_1G_2 are the projections of lines belonging to the solidus, as explained in the text. Open points indicate the composition of all studied samples. *A–A*, *B–B*, *C–C*, *D–D*, and *E–E* are selected slices of the diagram studied further with DTA (Figs. 5–7).

solutions at the temperature of preparation (i.e., 550–600°C).

With composition moving from MnV_2O_6 towards $LiVMoO_6$, or to the saturated solutions (K_1K_2 line), systematic shifts of X-ray reflections are observed. Figure 4 shows the variations in cell parameters a, b, c, β, $c \sin \beta$, and V with composition parameter Y, as determined for samples changing along the MnV_2O_6–$LiVMoO_6$ arm of the diagram (ML solutions). It can be seen that on passing from MnV_2O_6 to $LiVMoO_6$, the unit cell volume increases by 2.76%, and the dilation of b amounts to 3.11%. At the same time, c and $c \sin \beta$ decrease by 1.42 and 0.70%, respectively, and a changes insignificantly (0.37%). This is the expected trend, taking into account the ionic radii of components: $r_{Mn^{2+}} = 0.80$ Å, $r_{V^{5+}} = 0.54$ Å, $r_{Mo^{6+}} = 0.60$ Å, $r_{Li^{+}} = 0.74$ Å, $r_{O^{2-}} = 1.36$ (*13*), and the crystal structure of brannerite type (*1, 5, 14–19*). In this structure the VO_6 octahedra, sharing opposite corners, form chains parallel to the b axis. The lengths of the V–O bonds forming nearly linear –V–O–V–O–V– rows along these chains are

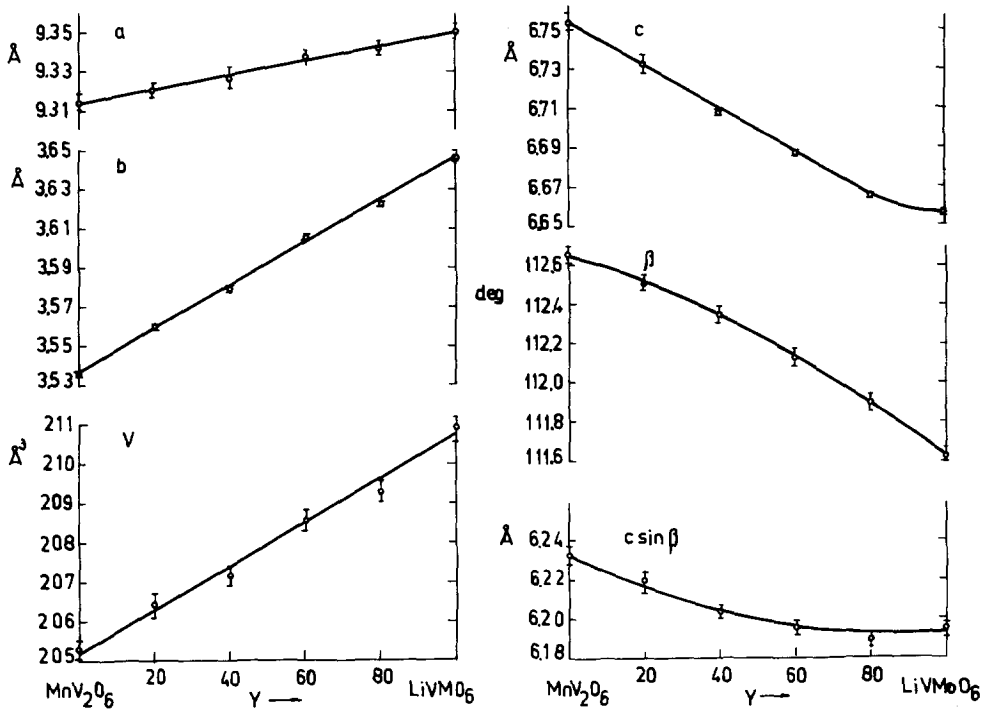

FIG. 4. Unit cell parameters vs Y in the $Mn_{1-y}Li_yV_{2-y}Mo_yO_6$ solid solutions (i.e., along the MnV_2O_6–$LiVMoO_6$ arm of the diagram). Confidence intervals are marked in the figure. They are ±0.001–±0.003 Å for a, b, c, and $c \sin \beta$, ±0.01–±0.02 deg for β, ±0.2–±0.3 for V.

equal to about 1.85 Å,[1] i.e., less than the sum of the ionic radii. VO_6 octahedra of the adjacent chains share edges, thus forming anionic sheets parallel to the (001) plane. The V–O bonds forming the double V–O–V bridges along the a axis form alternating bonds of about 1.7 and 2.7 Å, which indicates that the structure is much more loosely packed in the a direction than in the b direction. The A atoms are situated between anionic sheets in AO_6 octahedra forming chains paralleling the b axis, and not linked to one another. One thus expects that substitution of the larger Mo^{6+} ion for the smaller V^{5+} ion should primarily give rise to an increase of parameter b, corresponding to the direction of tight packing, while substitution of the smaller Li^{1+} for the larger Mn^{2+} ion should cause a decrease of parameter c and $c \sin \beta$, indicating the distance between the anionic sheets in the structure. The relative proportions of the above quoted ionic radii,

$$\frac{r_{Mo^{6+}} - r_{V^{5+}}}{r_{V^{5+}}} = 11.1\%$$

$$\frac{r_{Li^{1+}} - r_{Mn^{2+}}}{r_{Mn^{2+}}} = -7.5\%$$

suggest that the first effect should be more important, which is, in fact, observed experimentally. For the same reason, the volume of unit cell increases on passing from MnV_2O_6 to $LiVMoO_6$, but less so than the parameter b. As for a, the opposing effects

[1] The structures of MnV_2O_6 and $LiVMoO_6$ have never been resolved, but a series of papers (*5, 14–19*) indicates that the sets of V–O distances in VO_6 groups of various vanadates crystallizing in the brannerite type are practically the same.

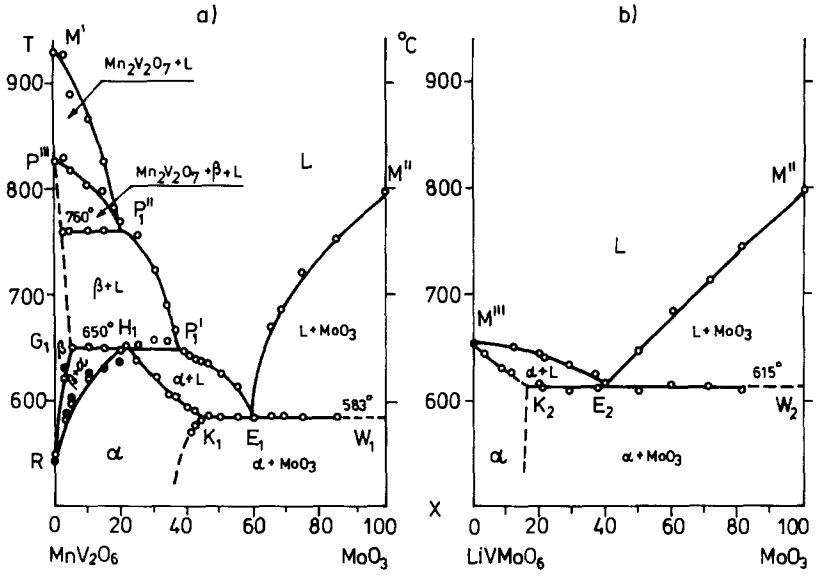

FIG. 5. Temperature–composition diagrams for MnV_2O_6–MoO_3 and $LiVMoO_6$–MoO_3 systems. Open points indicate DTA, full points indicate high temperature X-ray analysis.

of the two kinds of simultaneous substitutions closely compensate one another.

(iii) Phase Diagram

The phase diagram of the pseudo-binary system MnV_2O_6–MoO_3 has been already determined in (*1*), and is recalled in Fig. 5(a). In the present investigations, based on DTA and high temperature X-ray analyses, temperature–composition diagrams are constructed for the pseudo-binary systems MnV_2O_6–$LiVMoO_6$ and $LiVMoO_6$–MoO_3, as well as for the arbitrary slices *A–A*, *B–B*, *C–C*, *D–D*, and *E–E* indicated in Fig. 3.

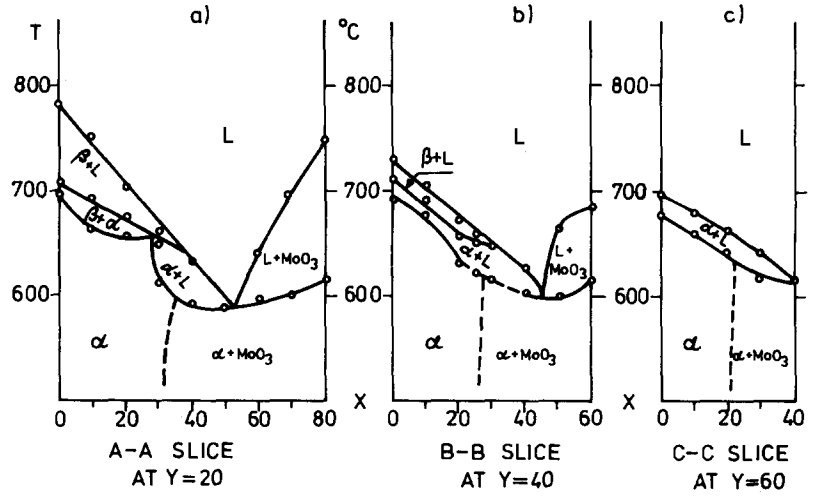

FIG. 6. Temperature–composition diagrams for *A–A*, *B–B*, and *C–C* slices of the MnV_2O_6–$LiVMoO_6$–MoO_3 system (cf. Fig. 3). Open points indicate DTA.

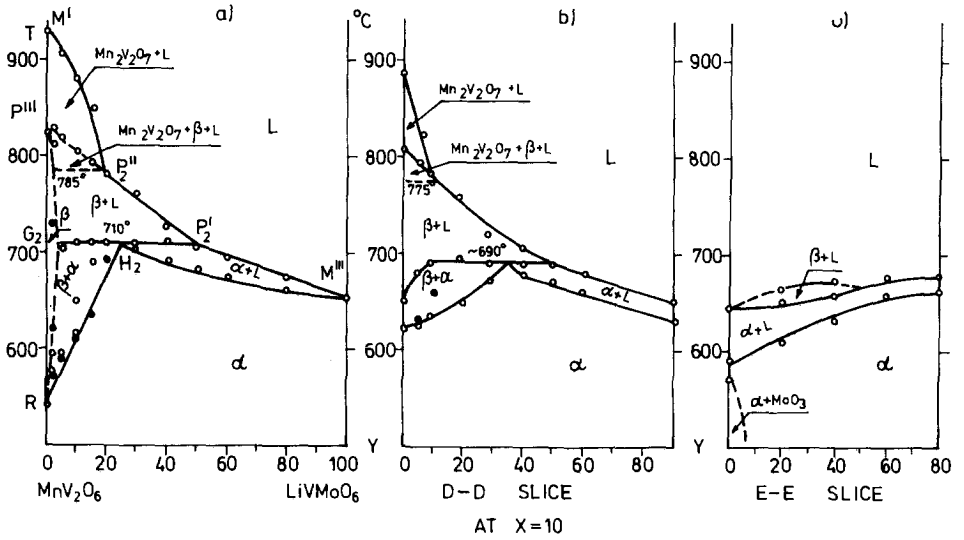

FIG. 7. Temperature–composition diagrams for the MnV_2O_6–$LiVMoO_6$ system and for *D–D* and *E–E* slices of the MnV_2O_6–$LiVMoO_6$–MoO_3 system (cf. Fig. 3). Open points indicate DTA, full points indicate high temperature X-ray analysis.

The results are presented in Figs. 5–7. They permit one to understand the shape of the whole pseudo-ternary *T*–MnV_2O_6–$LiVMoO_6$–MoO_3 diagram and, in particular, to determine (i) the upper temperature limit of stability of α-MLØ (Fig. 3), and (ii) the liquidus surfaces with isotherms (Fig. 8). Each isotherm is based at least on three experimental points, and in their determination, the DTA of samples lying outside of the slices shown in Figs. 5–7 are also used.

In describing the pseudo-ternary MnV_2O_6–$LiVMoO_6$–MoO_3 phase diagram it will be useful to take advantage of the previously studied MnV_2O_6 and MnV_2O_6–MoO_3 system (Fig. 5(a)) as a reference. As already discussed in (*1*), MnV_2O_6 is known to undergo a reversible phase transformation at *R*(0,0,540).[2] The low temperature α modification crystallizes in the brannerite type, while the structure of the high temperature β polymorph is not known (nonindexed powder X-ray pattern are presented in (*1*)). At *P‴*(0,0,825), β-MnV_2O_6 melts incongruently, decomposing to $Mn_2V_2O_7$ and liquid. The liquidus line in the MnO–V_2O_5 system, over MnV_2O_6, is attained at M′(0,0,935).

On doping MnV_2O_6 with MoO_3, solid solutions MØ are formed in both α and β modifications of MnV_2O_6. The extent of solid solubility in β-MnV_2O_6 is very small and attains its largest value at G_1(4,0,650). Contrarywise, the region of α-MØ extends up to K_1(45,0,583). In between there is an area of coexistence of α-MØ and β-MØ of different molybdena content, bordered by the "triangle" *R*(0,0,540)G_1(4,0,650) H_1(20,0,650). Doping stabilizes α-MØ against the α → β transformation. At H_1(20,0,650), α-MØ revealing the highest thermal stability among α-type solutions melts incongruently, decomposing to β-MØ and liquid, represented by G_1(4,0,650) and P'_1(37,0,650), respectively. Between 650 and 760°C one deals with a coexistence of slightly defective β-MØ G_1(4,0,650) *P‴*(0,0,825), and liquid P'_1(37,0,650)

[2] All particularly interesting points in the diagram are characterized (in parentheses) by three coordinates: *X*, *Y*, and *T* in °C.

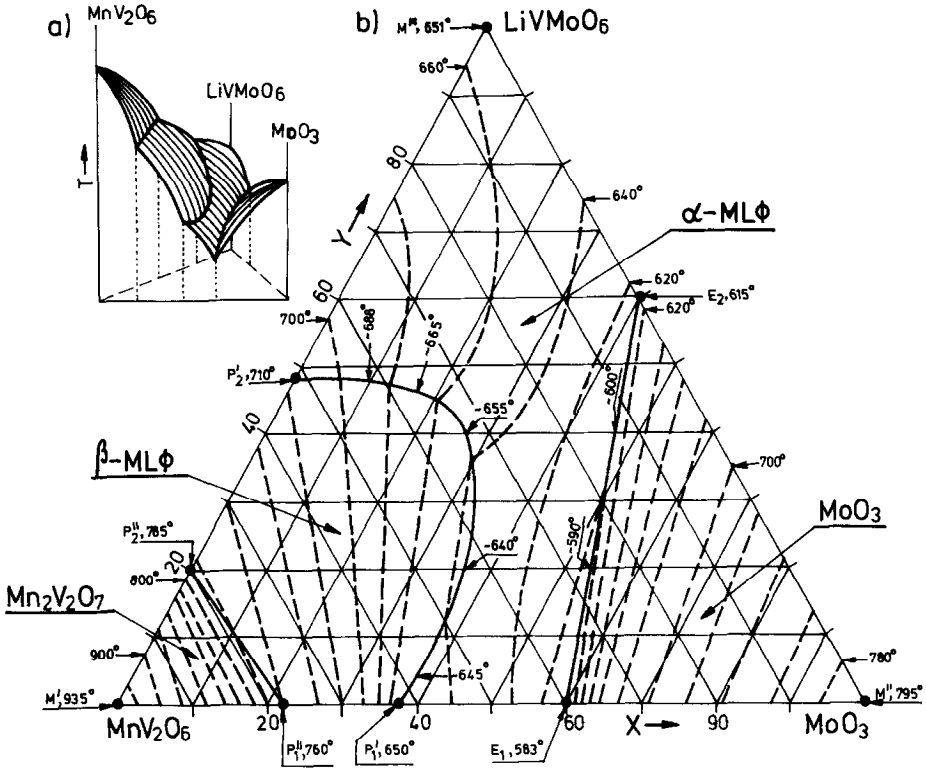

FIG. 8. Liquidus surfaces of the MnV_2O_6–$LiVMoO_6$–MoO_3 system. (a) Outline of the shape of liquidus; (b) projection based on DTA (cf. Figs. 5–7), with marked crystallization fields, and isotherms drawn every 20°C.

P'_1(22,0,760). At 760°C one enters the three phase area β-MØ + $Mn_2V_2O_7$ + liquid, and then the two phase area $Mn_2V_2O_7$ + liquid, wherein the composition of liquids changes along lines localized in the space of T–MnO–V_2O_5–MoO_3 diagram, P''_1(22,0,760) P'''(0,0,825) and P''_1(22,0,760)M'(0,0,935), these being their projections on the T–MnV_2O_6–MoO_3 plane, respectively (*1*). At higher MoO_3 content one eutectic appears in the system, where liquid represented by E_1(60,0,583) remains in equilibrium with MoO_3 and α-MØ, corresponding to K_1(45,0,583). P'_1(37,0,650)E_1(60,0,583) and E_1(60,0,583)M''(100,0,795) lines constitute the liquidus in this part of the diagram. MoO_3 melts at M''(100,0,795).

All the above-mentioned features of the flat T–MnV_2O_6–MoO_3 diagram are continued in the space of the T–MnV_2O_6–$LiVMoO_6$–MoO_3 diagram in which α-MLØ and β-MLØ solid solutions appear. The space of β-MLØ (Fig. 3) is bordered by two deformed conic-like surfaces extending between R(0,0,540), P'''(0,0,825) and a line which climbs from G_1(4,0,650) to G_2(0,4,710), the last point lying on the T–MnV_2O_6–$LiVMoO_6$ wall of the diagram (Fig. 7(a)). The tenative projection of the G_1G_2 line is shown in Fig. 3(b).

The space of α-MLØ (Fig. 3) expanding over about 50% of the basal composition triangle is covered with a "tent" built of two surfaces. The first extends between R(0,0,540) and a line joining H_1(20,0,650) with H_2(0,25,710), the last point lying on the T–MnV_2O_6–$LiVMoO_6$ wall of the diagram. The second extends between H_1H_2

and $K_1(45,0,583)K_2(16,84,615)$, the last point lying on the T–$LiVMoO_6$–MoO_3 wall. The melting point of $LiVMoO_6$, $M'''(0,100,651)$, also belongs to the second of the quoted surfaces. Projections of H_1H_2 and K_1K_2 are included in Fig. 3 and the original data in T-composition coordinates (for lateral and intermediary points of the discussed lines) may be found in Figs. 5–7.

The space of coexistence of α-MLØ and MoO_3 (Fig. 5(a,b)) is covered with a surface consisting of the $K_1(45,0,583)W_1(100,0,583)$ line and the $K_2(16,84,615)W_2(100,0,615)$ line. The temperature dependence of the boundary between α-MLØ and α-MLØ + MoO_3 spaces has not been exactly determined in this study. However, as the DTA patterns of samples lying near the boundary (see the respective slices in Fig. 6) agree with their phase composition at room temperature, one may conclude that this boundary is nearly vertical, especially in the vicinity of the T–$LiVMoO_6$–MoO_3 wall.

The shape of liquidus of the system is shown in Fig. 8. It is composed of four surfaces extending between the

(i) $M'(0,0,935)$ and $P_1''(22,0,760)$ $P_2''(0,20,785)$ line,

(ii) $P_1''P_2''$ and $P_1'(37,0,650)P_2'(0,50,710)$ lines,

(iii) $P_1'P_2'$ and $E_1(60,0,583)E_2(40,60,615)$ lines, and

(iv) E_1E_2 line and $M''(100,0,795)$ point.

The respective projections are shown in Fig. 8; the original data may be found in Figs. 5–7, as explained in detail for the solidus surfaces. It should be stressed that in analogy to the previously described T–MnV_2O_6–MoO_3 diagram, the first of the above-mentioned liquidus surfaces does not reflect the real compositon of liquid (it is a type of "projection" from the four-dimensional space), and that below it an additional surface exists (of the same character) between the $P'''(0,0,825)$ point and the $P_1''(22,0,760)P_2''(0,20,785)$ line. The last mentioned surface borders on the spaces of $Mn_2V_2O_7$ + liquid and $Mn_2V_2O_7$ + β-MLØ + liquid.

Finally, one may conclude that the pseudo-binary T–$LiVMoO_6$–MoO_3 diagram is the natural subdiagram of the ternary T–Li_2O–V_2O_5–MoO_3 or quaternary T–MnO–Li_2O–V_2O_5–MoO_3 diagrams in the whole range of temperature and composition. All tie lines are comprised in its plane, and thus all phase interactions and phase relations may be as easily deduced as for the true binary system. The same is true of the bidimensional T–MnV_2O_6–MoO_3 and T–MnV_2O_6–$LiVMoO_6$ diagrams, and for the three-dimensional T–MnV_2O_6–$LiVMoO_6$–MoO_3 diagram, but only below 760–785°C. Above these temperatures $Mn_2V_2O_7$ and liquid appear in the systems, the compositions of which cannot be expressed on their composition scales, as the respective tie lines pierce the planes or the space of the diagrams.

The outstanding feature of the phase diagram of the pseudo-ternary MnV_2O_6–$LiVMoO_6$–MoO_3 system is the very large range of stability of quaternary solid solution α-$Mn_{1-x-y}Li_y\emptyset_x$ $V_{2-2x-y}Mo_{2x+y}O_6$, in which y may vary between 0 and 1, and x between 0 and x_{max} ($0.16 \leq x_{max} \leq 0.45$), depending on y. The hypothesis as stated in the Introduction has thus been proved.

Acknowledgment

We are indebted to Dr. Roman Kozlowski who kindly pointed out to us the use of the citrate precursor method, and who performed some of the first syntheses of MØ solid solutions with this method.

References

1. R. KOZŁOWSKI, J. ZIÓŁKOWSKI, K. MOCAŁA, AND J. HABER, *J. Solid State Chem.* **35,** 1 (1980); Erratum **38,** 138 (1981).
2. J. ZIÓŁKOWSKI, R. KOZŁOWSKI, K. MOCAŁA, AND J. HABER, *J. Solid State Chem.* **35,** 297 (1980).

3. T. MACHEJ, R. KOZŁOWSKI, AND J. ZIÓŁKOWSKI, *J. Solid State Chem.* **38,** 97 (1981).
4. R. KOZŁOWSKI AND K. STADNICKA, *J. Solid State Chem.* **39,** 271 (1981).
5. B. DARRIET AND J. GALY, *Bull. Soc. Fr. Mineral. Crystallogr.* **91,** 325 (1968).
6. J. GALY, J. DARRIET, AND B. DARRIET, *C.R. Acad. Sci. Ser. C* **264,** 1477 (1967).
7. P. COURTY, H. AJOT, AND C. MARCILLY, *Powder Technol.* **7,** 21 (1973).
8. Joint Committee on Powder Diffraction Standards 1973, 5-508, 5-661, 9-387.
9. L. DZIEMBAJ AND J. ZIÓŁKOWSKI, *Bull. Acad. Pol. Sci. Ser. Sci. Chim.* **20,** 725 (1972).
10. T. MACHEJ AND J. ZIÓŁKOWSKI, *J. Solid State Chem.* **31,** 135 (1980).
11. N. F. CURTIS, *J. Chem. Soc.*, 3147 (1961).
12. P. W. SELWOOD, "Magnetochemistry," Interscience, New York/London (1956).
13. R. D. SHANNON AND C. T. PREWITT, *Acta Crystallogr.* **B25,** 925 (1969).
14. H. N. NG AND C. CALVO, *Canad. J. Chem.* **50,** 3619 (1972).
15. C. CALVO AND D. MANOLESCU, *Acta Crystallogr.* **B29,** 1743 (1973).
16. J. ANGENAULT, *Rev. Chem. Mineral.* **7,** 651 (1970).
17. E. E. SAUERBREI, M.S. Thesis, McMaster University, Ontario, Canada, (1972).
18. J.-C. BOULOUX AND J. GALY, *Bull. Soc. Chim. Fr.*, 736 (1969).
19. J. ZIÓŁKOWSKI, *J. Catal.* **80,** 263 (1983).